Success and breakdown of Tanner's law for drops of dense granular suspensions

Alice Pelosse, Élisabeth Guazzelli, Matthieu Roché

Under consideration for publication in J. Fluid Mech.

Success and breakdown of Tanner's law for drops of dense granular suspensions

Alice Pelosse†, Élisabeth Guazzelli and Matthieu Roché

Université Paris Cité, CNRS, Matière et Systèmes Complexes UMR 7057, F-75013, Paris

(Received xx; revised xx; accepted xx)

The spreading of viscous drops of density-matched suspensions on a solid surface is experimentally investigated at the global drop scale. The spreading dynamics still obeys Tanner's law provided one uses an effective viscosity which happens to be smaller than the bulk viscosity of the suspension. When the height of the drop is of the order of the particle size, Tanner's law breaks down as the particles start to freeze and the pure fluid drains out of the solid matrix.

Key words:

1. Introduction

The spreading of a liquid on a solid substrate is a common phenomenon, e.g. on plant leaves after the impact of raindrops or insecticide droplets, or during the coating of surfaces in industry. In these examples, the spreading fluid is not always a pure liquid as it may carry rigid bodies, such as fine dust particles in raindrops or solid particles added to the coating fluid. It is therefore of great importance to examine whether the spreading laws established for a pure fluid are still valid for such a complex fluid.

In this work, we focus on granular suspensions, a type of complex fluid extensively studied in bulk-flow situations, but quite unexplored when confined by a free interface such as for a spreading droplet. Granular suspensions are made of large particles (i.e. having diameter $d > 10\,\mu$m) such that Brownian motion and colloidal forces are negligible. Despite their high degree of heterogeneity at the microscopic scale, these particulate systems can be seen as continuous effective fluids at the macroscopic scale, with a bulk viscosity that solely depends on the particle volume fraction, ϕ, and is notably independent of particle diameter d for monodisperse rigid spheres (see e.g. Guazzelli & Pouliquen 2018).

Such a macroscopic description fails when the size of the system approaches that of the particle as seen in thin films (Palma & Lhuissier 2019; Gans *et al.* 2019) or near an advancing contact line (Zhao *et al.* 2020; Pelosse *et al.* 2023). In that latter case, the relation between the dynamic contact angle and the spreading velocity is similar to the classic Cox-Voinov law observed in the case of a pure liquid (Voinov 1976; Cox 1986). However, the wetting viscosity involved in this law differs from that of the bulk as it depends not only on ϕ but

† Email address for correspondence: alice.pelosse@gmail.com

also on d. This observation is linked to the ability of the particles to approach the contact line close enough to affect dissipation (Zhao *et al.* 2020; Pelosse *et al.* 2023).

In the present work, the spreading of viscous drops of density-matched suspensions (having a volume V_0, a surface tension with air γ, and a density ρ) on a solid surface is experimentally investigated at the global drop scale, i.e. by recording the time evolution of their radius, $R(t)$. For pure fluids, the radius growth is expected to follow Tanner's law (Tanner 1979) such that $R(t) = A\,t^n$, where both the factor A and the exponent n depend on V_0. For drop radii smaller than the capillary length, i.e. $R_0 \sim V_0^{1/3} < \ell_c = \sqrt{\gamma/\rho g}$ (with $\ell_c = 1.8\,\text{mm}$ in the present work), the spreading is driven by the balance of capillary and viscous forces, leading to $A \propto (V_0^3\gamma/\eta)^{1/10}$ and $n = 1/10$ (De Gennes 1985). Conversely, for large drops, i.e. $R_0 > \ell_c$, gravity prevails over capillarity and the spreading behaviour is established through the balance between gravity and viscous dissipation, resulting in $A \propto (V_0^3\rho g/\eta)^{1/8}$ and $n = 1/8$ (Lopez *et al.* 1976; Hocking 1983). This paper discusses the validity of Tanner's law for large drops of granular suspensions and compares the present dynamics at the global drop scale to that previously obtained at a local scale in the vicinity of the contact angle.

2. Experimental methods

Two different types of granular suspensions have been used in the experiments. The first combination of particles and fluid consists of spherical polystyrene beads (Dynoseeds TS, Microbeads, Norway) suspended in a density-matched Newtonian PEG copolymer [Poly(ethylene glycol-ran-propylene glycol) monobutyl ether] (Sigma) widely used in previous experimental work (see e.g. Guazzelli & Pouliquen 2018). The fluid density $\rho = 1056\ \text{kg/m}^3$ is close to that of polystyrene and its dynamic viscosity is measured to be $\eta_f = 2.4 \pm 0.1$ Pa.s at 22 °C. Different batches of particles are used with varying mean diameters $d = 20$, 40, 80, 140, 250 and 550 µm (with dispersion in size of 10%). The suspension mixture is made by weighting a mass of suspending fluid and adding the amount of solid needed to reach the desired particle volume fraction $\phi = 40$ % in most of the situations presented in §3. Larger loading in particles are also investigated as described in §3.4. Mixing is achieved by (i) first slowly stirring with a spatula and (ii) then using a rolling device overnight. The particles are found to be completely wet by the fluid and to experience no aggregation. The surface tension of the suspensions is that of the PEG copolymer, $\gamma = \gamma_f \simeq 35\,\text{mN m}^{-1}$, as confirmed by pendant drop experiments. The second type of suspension consists of 60-µm PMMA spheres (Spheromers CA, Microbeads, Norway) immersed in a fluid chosen to match the density and index of the particles. This fluid is a mixture of Triton X-100 (73 wt%), zinc chloride (16 wt%), and water (11 wt%) having a viscosity $\eta_f = 3.3 \pm 0.1$ Pa.s at 22 °C. A fluorescent dye, Rhodamine 6G, is added to the fluid to aid the visualisation with a laser sheet as described in §3.3. Only a single solid volume fraction of $\phi = 40$% has been studied for this suspension mixture.

Drops comprising the smallest particles (from 20 µm to 250 µm) are made using a syringe pump pushing the target volume of fluid at a flow rate 1 mL/min out of a 3 mm needle (inner diameter). To avoid transient heterogeneity in the suspension microstructure, at least 3 mL of suspension is discarded before any experiments. For the largest 550 µm particles, due to concerns about confinement effects in the tubing, the drops are made manually with a spatula ensuring a better control of ϕ. In all cases, the drops are deposited onto (Neyco Fused Silica) Quartz substrates carefully enough to produce axisymmetric spreading. To this extent, before each experiment, the substrate is cleaned thoroughly with deionised water and ethanol and treated with a plasma cleaner to avoid pining of the advancing contact line. Under these conditions, the continuous phase of the suspensions wets completely the surface of the wafer.

The spreading of the drop is recorded by a (Imaging Source) monochrome digital camera

(with a spatial resolution of 23 pixels/mm) located 50 cm above the solid substrate and operated at a frame rate of $1\,s^{-1}$ which provides a capture of both early and long-time dynamics. Automatic measurement of the radius is performed by a Python script that (i) first blurs locally the raw picture over roughly 5 pixels, (ii) then detects the edges of the drop using the (scikit-image toolbox) Canny edge detector with a Gaussian width of 1, and (iii) finally returns the best circle fitting the outer radius using the (scikit-image toolbox) Hough transform function. Additional side-view recording is performed by a camera positioned at a few centimetres from the drop (with spatial resolution of 0.6 µm/pixel) which is synchronised with the top-view camera. Post-treatment of the recording uses the Sobel filter to detect drop contour and extract the drop profile as a function of time (Pelosse *et al.* 2023).

In our experiments, the initial time is ill-defined, see figure 1(*a*). Indeed, as the drop touches the solid surface and starts spreading, it is attached to the needle for a certain amount of time which goes from a few seconds to one minute depending on the drop composition. The growth of the radius according to Tanner's law is therefore only investigated once the drop is fully detached from the needle, i.e. at a delayed time t_0. The radius data are therefore fitted with the parameterised function $R(t, t_0, A) = A(t + t_0)^{1/8}$, where $A = k(\rho g V_0^3/\eta_f)^{1/8}$ with k a constant, V_0 the drop volume inferred from its mass, and η_f the viscosity of the PEG copolymer measured by a capillary viscometer for each experiment. The fitted parameters t_0 and A are estimated numerically. An alternative method is to use an initial radius instead of an initial time, i.e. $R(t, R_0, A') = R_0 + A' t^{1/8}$ (Saiseau *et al.* 2022). This is equally efficient but we have chosen the time-offset correction in the present data analysis. For smaller drops, a transition from a (short-time) capillary to a (long-time) gravity regime has been reported (Cazabat & Cohen Stuart 1986; Levinson *et al.* 1988). Such changes in power law are not observed with the drop sizes investigated in the present work. It should be stressed that the time offset correction only affect the behaviour at short time and does not modify that at long time which is undoubtedly driven by gravity with a power law exponent of 1/8 as evidenced in figure 1(*a*) discussed in § 3.1.

3. Results

3.1. *Tanner's law*

Figure 1(*a*) shows the typical time-evolution of the radius of drops consisting of pure fluid and granular suspensions. The colour coding indicates the different fluids while the symbol coding the varying drop volume. The raw data are plotted versus time t in the inset whereas the main graph displays the normalised radius $R^* = R(\eta_f/V_0^3)^{1/8}$ versus $t + t_0$. This radius normalisation removes volume and viscosity effects, as evidenced by the tight collapse of the curves for a given fluid. The time offset corrects the initial bending seen in the inset as already explained at the end of § 2. The spreading clearly obeys a gravity-driven dynamic, i.e. $R \sim t^{1/8}$, as expected for the relatively large Bond numbers considered, $2.6 \leqslant Bo = (3V_0/4\pi)^{2/3}/\ell_c^2 \leqslant 11.9$. Drops of suspensions of any volume and concentration seem to obey Tanner's law established for continuous Newtonian fluids. However, there are two main differences. First, the curves of the main log-log plot for suspension drops exhibit a small vertical shift compared to those for the pure fluid which indicates that the factor A of Tanner's law differs when adding particles to the fluid. Second, for the largest particles ($d = 550$ µm), the dynamic slows down for $t \gtrsim 200$ s. Deviations from Tanner's law will be successively discussed in the following § 3.2 and 3.4.

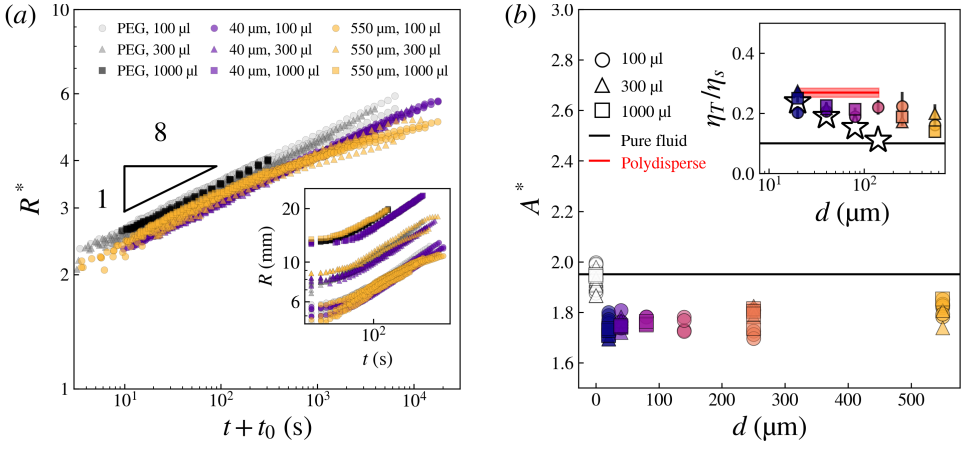

Figure 1: (*a*) Normalised radius $R^* = R(\eta_f/V_0^3)^{1/8}$ versus time (with the t_0 offset) for different drop volume V_0 =100, 300, and 1000 µL and different fluids: suspensions with $d = 40$ µm (purple symbols) and 550 µm (gold symbols) at $\phi = 40\%$ and pure PEG (grey and black symbols). Inset: raw data of the radius versus time. (*b*) Normalised factor $A^* = A(\eta_f/V^3)^{1/8}$ versus particle diameter d (from 20 µm to 550 µm). The open symbols correspond to experiments with pure PEG. Inset: ratio of the relative effective viscosity obtained from Tanner's law, η_T, to the relative bulk viscosity, η_s, versus particle diameter d. The red horizontal line corresponds to this ratio for a polydisperse suspension made of particles of 20 µm, 40 µm, 80 µm and 140 µm, each size representing 10 % of the suspension volume. The star symbols corresponds to the relative effective wetting viscosity of the same suspensions obtained from the Cox-Voinov law (Zhao *et al.* 2020).

3.2. *Tanner's effective viscosity*

We start by discussing the impact of adding particles on the factor A. In the main graph of figure 1(*b*), the normalised factor, $A^* = A(\eta_f/V_0^3)^{1/8}$, is plotted for all the experiments. This normalisation eliminates any V_0-dependence for a given fluid. We see that the value of A^* is smaller for suspensions than for the pure continuous phase and its value is roughly independent of d. The viscosity of the continuous phase η_f used to compute A^* underestimates the viscosity of the suspensions. Seeking to compare the effective viscosity inferred from Tanner's law with its bulk counterpart, we write the Tanner suspension viscosity as $\eta_T\eta_f$. To shift the suspension data onto the solid line corresponding to the PEG data in the figure 1(*a*), the relative viscosity η_T should be computed as $\eta_T = (\rho g/\eta_f V_0^3)(k/A)^8$, where $k = 0.61 \pm 0.02$ has been inferred from the pure PEG data (open symbols) using $A^*_{PEG} = k(\rho g)^{1/8} = 1.94$. This relative viscosity extracted from Tanner's law is reported in the inset of figure 1(*b*) for the different suspensions and drop volumes. It is found to be independent of d and V_0 with a value $\eta_T = 2.2 \pm 0.5$.

This relative Tanner viscosity η_T which describes the global dynamics of the drop differs from the relative wetting viscosity η_w extracted from the Cox-Voinov law found in the viscous–capillary region corresponding to the very close vicinity of the contact line, see the star symbols on the inset of figure 1(*b*). In contrast with the constant behaviour of η_T, η_w decreases with increasing d and reaches a value of one (that corresponding to the pure fluid) for a cut-off size (≈ 100 µm) above which particles are too large to affect dissipation in this region close to the contact line (Zhao *et al.* 2020; Pelosse *et al.* 2023). This difference between η_w and η_T may not come as a surprise as it derives from two different energy balances at the local and global scales, i.e. from a balance of capillary and viscous forces at the local scale of the contact line and of gravity and viscous forces at the global scale of the drop.

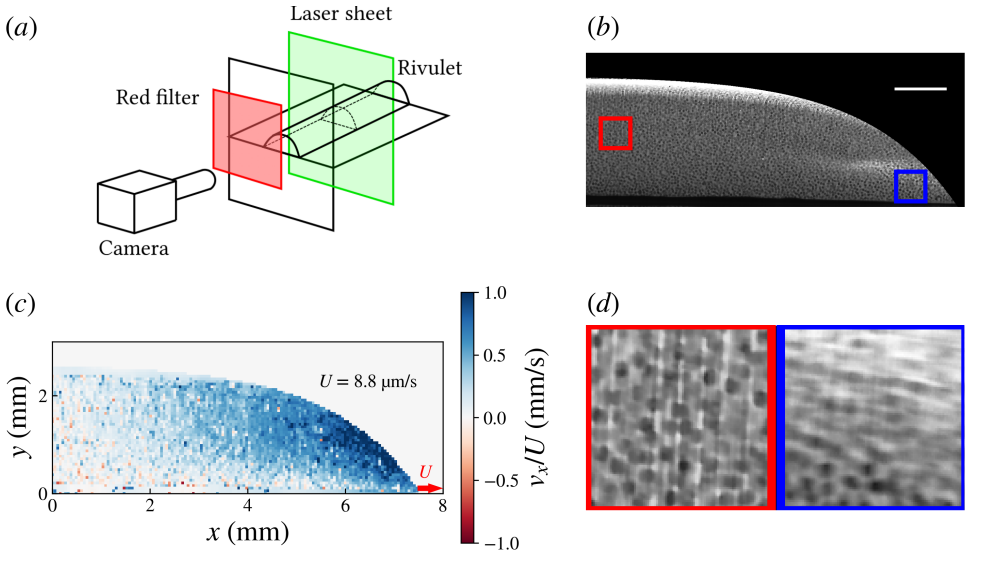

Figure 2: (*a*) Sketch of the apparatus used to visualize the particle flow in a spreading rivulet with a laser sheet. A fluorescent dye suspended in the fluid is excited by the green light and fluoresces red light collected by a side view camera. (*b*) Imaging for a suspension made of 60-µm particles at $\phi = 40\%$ (scale bar: 1 mm). See accompanying movie 1 in the supplementary material. (*c*) Horizontal speed v_x from PIV analysis of the particle flow in (*b*). The speed is normalised by the contact line velocity U. (*d*) Sum of raw pictures between t and $t + \Delta t$ with $\Delta t = 2d/U$ in the corresponding red (left) and blue (right) squares in subplot (*b*).

The Tanner viscosity happens also to be much smaller than the bulk viscosity of the suspension as the relative bulk viscosity is $\eta_s \simeq 10$ at the same $\phi = 40\%$. This may be due to particle slip along the very smooth substrate. Another difference may come from the suspension microstructure which certainly is dissimilar in the present non-viscometric flow and in a pure shearing flow. Besides, confinement by both the substrate and the mobile interface may create layering that could span over 10 particle diameters at $\phi = 40\%$ (Gallier *et al.* 2016) and end up in a strong dip in dissipation (Ramaswamy *et al.* 2017). However, experiments with polydisperse suspensions do not support this explanation as suspensions consisting of a mixture of 20, 40, 80, and 140 µm particles (meant to hinder crystallisation) do not exhibit a significant increase in dissipation, see red line in the inset in figure 1(*b*). To discriminate between possible causes of this smaller value of η_T, we examine in detail the particulate flow during spreading in the following § 3.3.

3.3. *Visualisation of the particulate flow in the rivulet configuration*

To gain further insight into the particle motion during spreading, particle imaging is performed in a more convenient rivulet configuration, i.e. for a non-isotropic spreading along only one direction, using a density and index-matched suspension described in § 2. As sketched in figure 2(*a*), imaging without optical distortion is achieved using two orthogonal microscope slides. A green laser sheet (Coherent lasers, $\lambda = 532$ nm, 50 mW) illuminates the fluid rivulet through the bottom slide and a side view camera images the flow. The laser sheet is not deflected across the flat walls nor in the index-matched suspension and induces fluorescence of Rhodamine 6G in the illuminated slice (about 30 µm thick) which is excited by the green light and emits red wavelengths. This light is filtered by a high-pass red filter (Thorlabs, $\lambda > 550$ nm) and collected by the monochrome camera (Imaging

Source, DMK33UX174, 2.3 MP) mounted with a zero distortion lens (Opto Engineering, MC100X), and orthogonal to the laser sheet. The spatial resolution is of 3 µm/pixel and the acquisition frame-rate of 1 s^{-1}. With this apparatus, the non-fluorescing particles appear dark in the illuminated slice as seen in figure 2(b) and the accompanying movie. The horizontal speed coming from the PIV analysis of a frame is displayed in figure 2(c). The analysis is performed with the trackpy module of Python on two consecutive frames. The algorithm uses an interrogation window size of 16 pixels, a search area size of 18 pixels, and an overlap of 9 pixels. The velocity is normalised by the speed of the advancing contact line (red arrow). In figure 2(d), the sum of the pictures between t and $t + \Delta t$ is shown for $\Delta t = 2d/U$ in two specific regions. With this time interval, particles moving at a speed close to that of the contact line should not appear as fixed dark dots but should be blurred.

Visualisation of the particulate flow during the spreading of the suspension rivulet unveils several significant elements. Importantly, figure 2(b) and its accompanying movie do not exhibit any clear development of layering or ordering during spreading, meaning that particle self-organisation cannot explain the strong decrease in viscosity as that reported by e.g. Ramaswamy *et al.* (2017). However, PIV measurements presented in figure 2(c) and the sum of consecutive pictures in figure 2(d) reveal two crucial features of the particle flow. First, a strong particle slip develops along the wall near the advancing contact line as shown by the velocity signal in figure 2(c) or by the smearing of dark dots near the rivulet edge in figure 2(d) (right). Second, in the centre of the rivulet, particles barely move as illustrated by the weak velocity signal from the PIV in figure 2(c) or by the sum of the pictures in figure 2(d) (left). In this later figure, sharp dots at the centre of the rivulet (i.e. on the left) indicate that the particles have not moved within the time interval $\Delta t = 2d/U$, in contrast with the observations near the contact line (i.e. on the right) where the particulate phase undergoes a strong flow.

These observations of the structure of the particulate flow can explain the low value of the effective spreading viscosity displayed in the inset of figure 1(b). In rheometers, slip velocity of the particles leads to a smaller stress on the particles and results in an effective smaller viscosity (Jana *et al.* 1995; Yoshimura & Prud'homme 1988; Ahuja & Singh 2009). In spreading experiments, particles close to the tip of the rivulet exhibit a strong slip at roughly the contact line speed. This slip is not surprising under such strong confinement and given the very smooth surface of the solid substrate. Yet, slip by itself cannot account for such a large decrease in effective viscosity. This decrease could also be the result of the almost frozen particulate phase at the centre of the rivulet such that particles act more like a porous medium than like a flowing suspension in this region. Interestingly, the effective viscosity of a granular bed is found to be independent of particle size and to possess a value close to the Einstein viscosity ($\eta_s = 1 + 2.5\phi = 2$ at $\phi = 0.4$), i.e. a value much smaller than that of a sheared dense suspension due to the screening of the hydrodynamic interactions (Vowinckel *et al.* 2021). This bears a striking resemblance to the behaviour of η_T in figure 1(b). In summary, slip at the tip of the drop and porous-like behaviour at the centre of the drop/rivulet could both account for the observed η_T.

3.4. *Long time behaviour: validity of Tanner's law*

We now turn to the slowdown of the spreading dynamics observed above 200 s for suspensions made of the largest 550-µm particles. In figure 3, top view pictures of drop spreading evidence different patterns for suspensions having different particle size of 40 µm, 250 µm and 550 µm at $\phi = 40\%$. For the largest particles, top-views at a higher volume fraction, namely $\phi = 47\%$, are also presented on the last row (d). Clearly, the particle phase initially spreads with the fluid but then does not expand further beyond a critical radius which decreases with increasing particle size, as depicted on the first three rows (a), (b), (c), and with increasing particle

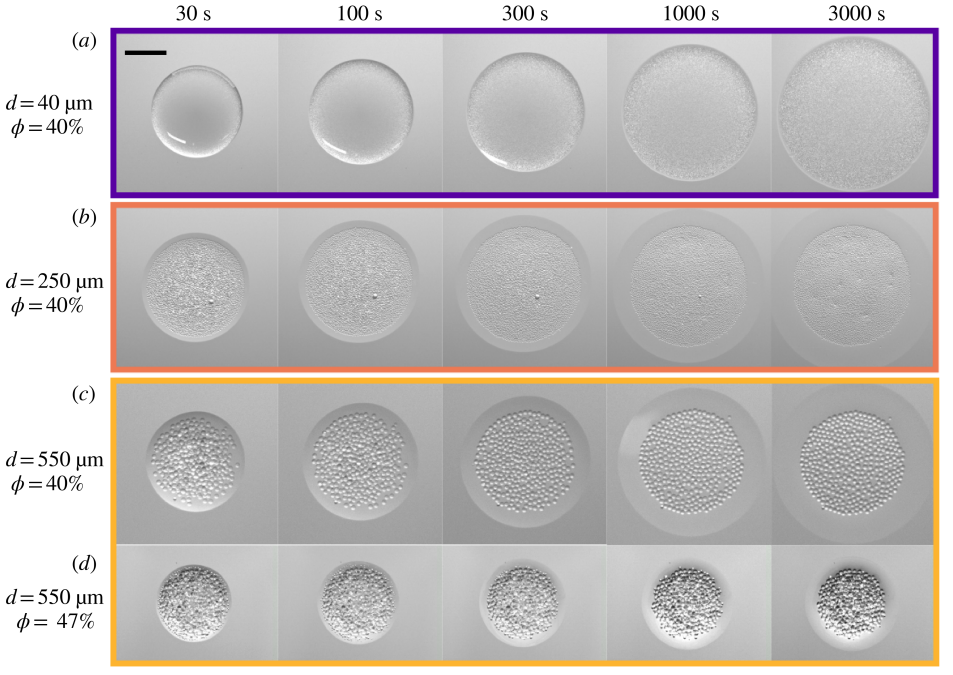

Figure 3: Top view pictures of the spreading of different suspensions. From top to bottom: (*a*) $d = 20\,\mu$m, $\phi = 40\%$; (*b*) $d = 250\,\mu$m, $\phi = 40\%$; (*c*) $d = 550\,\mu$m, $\phi = 40\%$; (*d*) $d = 550\,\mu$m, $\phi = 47\%$ (scale bar: 5 mm). See accompanying movie 2 in the supplementary material.

volume fraction, as shown on the two last rows (*c*), (*d*). There is a striking difference between the behaviour for the smallest particles where the particle arrest is barely seen (top row) and that for the largest particles (bottom row) where particle freeze happens at very early stage. These observations suggest that the departure from Tanner's law can be associated with the freezing of the particle matrix while the fluid continues to drain outward.

In figure 4(*a*), the fluid radius R of a 100 µL drop of a suspension consisting of 550 µm particles is plotted as a function of time (black solid line). The particle spreading radius, R_p, defined in the top left inset, is also plotted with a yellow solid line. Side-view snapshots numbered from (i) to (iv) taken during this spreading illustrate two different regimes. First, for pictures (i) and (ii), the drop profile is concave and R_p increases, meaning that particles move with the fluid, in agreement with the early time dynamics in figure 3. In this regime, the drop radius growth obeys Tanner's law and the suspension behaves like a continuous fluid. Second, while the contact line still progresses from (ii) to (iv), R_p saturates, i.e. the particles do not move and remain at the centre of the drop, also in agreement with observations from figure 3. This translates into a significant slowdown of the drop radius growth R and departure from Tanner's law (black solid line). In this second regime, the continuous approach fails and the fluid drains out of the porous matrix consisting of the large particles. The drop profile then takes a convex shape near the edge to connect the contact line with the centre of the drop where the particles remain, as seen in the thumbnails (iii) and (iv). In these pictures, the particle protrusions become more significant and one can clearly identify a single monolayer of particles in the picture (iv). Time evolution of normalised particle radii for drop consisting of different particle sizes and volume fractions are plotted in figure 4(*b*). The same normalisation to remove volume and viscosity effects is used and the drop volumes are kept similar at approximately 100 µL. This graph confirms that particle freezing happens

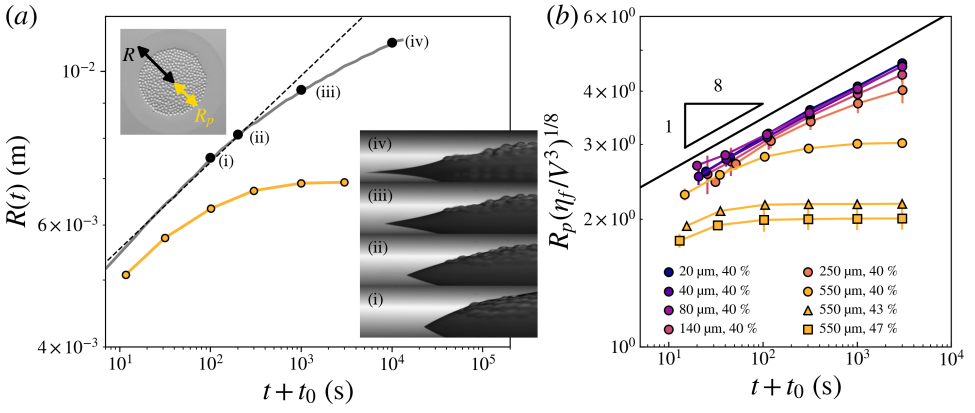

Figure 4: (a) Drop of suspension consisting of 550-µm particles with $V_0 = 100$ µL. Main graph: fluid radius R (black) and particle radius R_p (yellow) as a function of time. The dashed line correspond to Tanner's law. Thumbnails (i) to (iv): side-view pictures corresponding to the black dots in the main graph. Top inset: top view picture with fluid (R) and particle (R_p) radii. (b) Particle radius R_p as a function of time for different suspensions (see legend) with a drop volume $V_0 \simeq 100$ µL. Error bars are computed from standard deviations over different experiments.

earlier with large particles and large volume fractions. Conversely, for particle diameters $\lesssim$100 µm, R_p follows a power law growth with an exponent 1/8, i.e. the same dynamics as that predicted for a continuous fluid by Tanner's law.

To gain insight on the transition between these two regimes, the shape and thickness of the drop have been investigated. In figure 5(a, b), plots of the time-evolution of the profile $h(r,t)$, of the radius R, and of the drop-centre thickness h_0, for a drop of pure fluid (r is the radial distance from the drop centre) indicate that experimental profiles are well captured by the predictions of Hocking (1983) for Bond numbers $Bo = O(1)$,

$$h(r,t) = \frac{V}{\pi R(t)^2} \frac{I_0\left(\frac{R(t)}{\ell_c}\right) - I_0\left(\frac{r}{\ell_c}\right)}{I_2\left(\frac{R(t)}{\ell_c}\right)}, \tag{3.1}$$

where $I_n(x)$ is the n-th modified Bessel function of the first kind. In figure 5(b), the radius data (computed from top views) are fitted with Tanner's law (red dashed line) and used to compute the drop central thickness, h_0, according to (3.1) (blue dashed line). Excellent agreement is found with drop thickness data extracted from side views. Figure 5(a) shows the drop profiles extracted from these side views and the comparison with (3.1) at the times indicated by the large dots in figure 5(b). While not perfect, the agreement between the experimental and theoretical profiles is satisfactory, especially in predicting the central drop thickness. Side-views are therefore not required and drop profiles can be inferred using the drop radius $R(t)$ from top-view pictures.

The simplest criterion that can be proposed is that the breakdown of Tanner's law for granular suspensions happens when the drop thickness reaches approximately a particle diameter, as suggested by the side-view thumbnails in figure 4(a) where drop thickness is roughly 2-diameter thick at the transition for the 550-µm particles. This can be estimated by evaluating the time t_c (or equivalently the drop radius R_c) for which the central thickness $h_0(R_c) \simeq d$ with $R_c = At_c^{1/8}$. Figure 5(c) show that a nice collapse of drop radius versus time can be obtained for different particle sizes and drop volumes by normalising the radius by the critical radius R_c and the time by the critical time t_c. Spreading deviates from Tanner's law

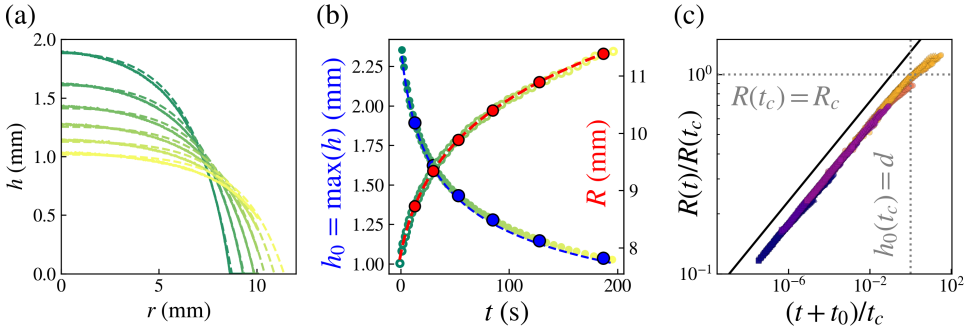

Figure 5: Spreading of a drop of pure fluid with $V_0 = 295$ µL. (a) Experimental profiles from side views (solid lines) and predicted shapes (dashed lines) from (3.1). The colour gradation indicates the time progression. The large dots in (b) correspond to the moments of the profiles plotted in (a). (b) Right axis: experimental radius R as a function of time and Tanner's law (red dashed line) with the fitted parameters $A = 0.0059$, $t_0 = 10.4$ s. Left axis: central thickness h_0 as a function of time with the prediction of (3.1) (blue dashed line). (c) Radius as a function of time, normalised by R_c and t_c, respectively, with $R_c = At_c^{1/8}$ and $h_0(R_c) = d$ (see legend in figure 1 for the symbols).

(solid line) for $t \simeq t_c$ for the 250 and 550 µm particles when $R \simeq R_c$. For the smallest particle diameter, the experiments are too short to observe the deviation as the critical thickness $h_0 = d$ is far from being reached.

4. Concluding remarks

A global-scale investigation of the spreading of a drop of granular suspension has been performed in the dense regime ($\phi \geqslant 40\%$) in order to exhibit the strongest effects of the particle phase. The first major output, developed in § 3.2, is that Tanner's law which describes the growth of the drop radius is still valid provided one uses an effective viscosity independent of the particle size. This so-called Tanner viscosity is much smaller than the bulk viscosity of the suspension probably due to the combined effect of particle slip near the tip of the drop and porous-like behaviour at the centre of the drop as shown by flow visualisation and PIV analysis in § 3.3. The second important finding is that, when the height of the drop becomes of the order of the particle spacing, the spreading slows down. This departure from Tanner's law comes from particle freezing and drainage of the pure fluid out of the porous particle matrix. In § 3.4, simply stating that this transition happens when the drop thickness reaches a particle diameter, $h_0(t_c) = d$, provides a decent prediction of the breakdown of Tanner's law at a solid volume fraction $\phi = 40\%$. However, a ϕ-dependent criterion (which is difficult to measure) is expected in view of the earlier particle freezing seen at larger ϕ in figure 4(b), i.e. as ϕ becomes closer to a jamming volume fraction upon spreading, ϕ_c^s, which is certainly lower than the usual bulk jamming volume fraction because of confinement (Scott & Kilgour 1969; Desmond & Weeks 2009). We anticipate a weak algebraic divergence with the distance to the jamming point similar to that found for the transition neck diameter in the pinch-off of a viscous suspension thread (Château *et al.* 2018). A tentative criterion could then be $h_0(t_c) = d/(\phi_c^s - \phi)^\alpha$ with $\alpha \simeq 1/3$ and could help to rationalise the earlier freezing when ϕ is close to ϕ_c^s. The spreading of granular drops and its transition from a continuous effective fluid to a discrete system is therefore the signature of a confinement-dependent jamming.

Supplementary data. Supplementary material and movies are available at https://doi.org/10.1017/jfm.2023...

Acknowledgements. We would like to thank two interns, Maël Lebon and Siham Mekel, for their precious help at the beginning of this project.

Declaration of interests. The authors report no conflict of interest.

Author ORCIDs.
Alice Pelosse https://orcid.org/0000-0002-4554-0604;
Élisabeth Guazzelli http://orcid.org/0000-0003-3019-462X;
Matthieu Roché http://orcid.org/0000-0002-8293-7029.

REFERENCES

Ahuja, A. & Singh, A. 2009 Slip velocity of concentrated suspensions in couette flow. *J. Rheol.* **53** (6), 1461–1485.

Cazabat, A.-M. & Cohen Stuart, M. A. 1986 Dynamics of wetting: effects of surface roughness. *J. Phys. Chem.* **90** (22), 5845–5849.

Château, J., Guazzelli, É. & Lhuissier, H. 2018 Pinch-off of a viscous suspension thread. *J. Fluid Mech.* **852**, 178–198.

Cox, R. G. 1986 The dynamics of the spreading of liquids on a solid surface. Part 1. Viscous flow. *J. Fluid Mech.* **168**, 169–194.

De Gennes, P.-G. 1985 Wetting: statics and dynamics. *Rev. Mod. Phys.* **57** (3), 827.

Desmond, K. W. & Weeks, E. R. 2009 Random close packing of disks and spheres in confined geometries. *Phys. Rev. E* **80** (5), 051305.

Gallier, S., Lemaire, É, Lobry, L. & Peters, F. 2016 Effect of confinement in wall-bounded non-colloidal suspensions. *J. Fluid Mech.* **799**, 100–127.

Gans, A., Dressaire, É., Colnet, B., Saingier, G., Bazant, M. & Sauret, A. 2019 Dip-coating of suspensions. *Soft matter* **15** (2), 252–261.

Guazzelli, É. & Pouliquen, O. 2018 Rheology of dense granular suspensions. *J. Fluid Mech.* **852**, P1.

Hocking, L. M. 1983 The spreading of a thin drop by gravity and capillarity. *Q. J. Mech. Appl. Math.* **36** (1), 55–69.

Jana, S. C., Kapoor, B. & Acrivos, A. 1995 Apparent wall slip velocity coefficients in concentrated suspensions of noncolloidal particles. *J. Rheol.* **39** (6), 1123–1132.

Levinson, P., Cazabat, A.-M., Cohen Stuart, M. A., Heslot, F. & Nicolet, S. 1988 The spreading of macroscopic droplets. *Rev. Phys. Appl* **23** (6), 1009–1016.

Lopez, J., Miller, C. & Ruckenstein, E. 1976 Spreading kinetics of liquid drops on solids. *J. Colloid Interface Sci.* **56** (3), 460–468.

Palma, S. & Lhuissier, H. 2019 Dip-coating with a particulate suspension. *J. Fluid Mech.* **869**, R3.

Pelosse, A., Guazzelli, É. & Roché, M. 2023 Probing dissipation in spreading drops with granular suspensions. *J. Fluid Mech.* **955**, A7.

Ramaswamy, M., Lin, N., Leahy, B., Ness, C., Fiore, A., Swan, J. & Cohen, I. 2017 How confinement-induced structures alter the contribution of hydrodynamic and short-ranged repulsion forces to the viscosity of colloidal suspensions. *Phys. Rev. X* **7** (4), 041005.

Saiseau, R., Pedersen, C., Benjana, A., Carlson, A., Delabre, U., Salez, T. & Delville, J.-P. 2022 Near-critical spreading of droplets. *Nat. Commun.* **13** (1), 7442.

Scott, G. D. & Kilgour, D. M. 1969 The density of random close packing of spheres. *Journal of Physics D: Applied Physics* **2** (6), 863.

Tanner, L. H. 1979 The spreading of silicone oil drops on horizontal surfaces. *J. Phys. D* **12** (9), 1473.

Voinov, O. V. 1976 Hydrodynamics of wetting. *Fluid Dyn.* **11** (5), 714–721.

Vowinckel, B., Biegert, E., Meiburg, E., Aussillous, P. & Guazzelli, É. 2021 Rheology of mobile sediment beds sheared by viscous, pressure-driven flows. *J. Fluid Mech.* **921**, A20.

Yoshimura, A. & Prud'homme, R. K. 1988 Wall slip corrections for couette and parallel disk viscometers. *J. Rheol.* **32** (1), 53–67.

Zhao, M., Oléron, M., Pelosse, A., Limat, L., Guazzelli, É. & Roché, M. 2020 Spreading of granular suspensions on a solid surface. *Phys. Rev. Res.* **2** (2), 022031.